Evaluation of a Coupled Wave-Ice Model in the Western Arctic

Vincent T. Cooper[1], Lettie A. Roach[1], Jim Thomson[2,3], Samuel D. Brenner[2], Madison M. Smith[2], and Cecilia M. Bitz[1]

[1]Department of Atmospheric Sciences, University of Washington
[2]Applied Physics Laboratory, University of Washington
[3]Department of Civil and Environmental Engineering, University of Washington

Key Points:

- We compare in situ observations of ocean surface waves in the Beaufort Sea with a coupled wave-ice model
- Locally generated wind waves are observed more than 100 km within pack ice, but the model lacks the resolution to generate waves in leads
- Swell is not observed more than 100 km within pack ice, but the model predicts that swell can persist at least this far in the Beaufort Sea

Corresponding author: Vince Cooper, `vcooper@uw.edu`

Abstract

The retreat of Arctic sea ice is enabling increased ocean surface wave activity at the sea ice edge, yet the physical processes governing interactions between waves and sea ice are not fully understood. Here, we use a collection of in situ observations of waves in ice to evaluate a recent global climate model experiment that includes coupled interactions between ocean waves and the sea ice floe size distribution. Observations come from subsurface moorings and free-drifting buoys spanning 2012-2019 in the Beaufort Sea, and we group the data based on distance inside the ice edge for comparison with model results. Locally generated wind waves are relatively prevalent in observations beyond 100 km inside the ice but are absent in the model. Low-frequency swell, however, is present in the model, while subsurface moorings located more than 100 km inside the ice do not report any swell with significant wave height exceeding the instruments' detection limits. These results motivate further model development and future observing campaigns, suggesting that local wave generation inside the ice edge may play a significant role for floe fracture while demonstrating a need for more robust constraints on wave attenuation by sea ice.

Plain Language Summary

Sea ice, the frozen surface water of polar oceans, is retreating toward the pole in the Arctic Ocean. The increase in open-ocean area around remaining sea ice enables bigger ocean waves, which can travel into sea ice and break ice into smaller pieces. Currently, climate models do not include ocean waves and their impacts on sea ice. In this study, we compare field observations with a model that simulates interactions between waves and sea ice. The observations, spanning 2012-2019 in Arctic waters north of Alaska, come from underwater instruments and floating buoys where the ocean surface is partially ice-covered. We check for differences in wave height, how wave energy is distributed between short and long wavelengths, and whether waves are generated by local winds. We find that local wind waves generated in partial sea ice cover appear in observations but not in the model. Separately, waves generated outside of sea ice that later traveled into ice cover are present in the model but not in observations beyond 100 km inside the ice. Local wave generation in sea ice may be important for changes in ice cover, and these results motivate model development and future observations.

1 Introduction

As the retreat of Arctic sea ice promotes increased ocean surface wave activity (Thomson & Rogers, 2014), interactions between waves and sea ice could play an elevated role in the Arctic climate system. Increasing wave heights have already been observed in the Beaufort Sea where fetch, the open water distance available for wave development, has expanded due to seasonal sea ice loss (X. L. Wang et al., 2015; Liu et al., 2016; Thomson et al., 2016; Smith & Thomson, 2016). Summer sea ice is also becoming less compact near the newly exposed, rougher seas that surround the remnant of sea ice left in the central Arctic (Martin et al., 2014; Thomson, Ackley, et al., 2018; Squire, 2020).

When waves encounter sea ice floes, distinct masses of ice ranging in size from meters to hundreds of kilometers, the ice scatters and dissipates wave energy (Wadhams et al., 1988; Squire et al., 1995; Squire, 2007; Kohout et al., 2014; Meylan et al., 2014; Montiel et al., 2016; Squire, 2020). In turn, ocean surface waves break large ice floes into smaller floes (Mellor et al., 1986; Meylan & Squire, 1994; Langhorne et al., 1998; Marko, 2003; Toyota et al., 2006; Collins et al., 2015), and during freezing conditions, waves can inhibit the formation of an extensive ice sheet by forcing frazil ice crystals to weld into small floes (Shen et al., 2001, 2004; Roach, Smith, & Dean, 2018). The interaction between waves and sea ice could cause a positive feedback: wave-induced ice fracture increases the lateral melt potential of floes by exposing more perimeter (Steele, 1992), melting the sea ice cover and facilitating further wave propagation (Kohout et al., 2011; Asplin et al., 2012, 2014; Horvat et al., 2016; Smith et al., 2021).

Interactions between waves and sea ice occur in the marginal ice zone (MIZ), the partially ice-covered region that separates interior pack ice from open ocean. We do not have direct estimates of the MIZ's location and extent because measuring waves in ice at basin scale is an ongoing challenge. While the physical significance of the dynamic MIZ stems from wave presence near the ice edge, a practicable proxy based on intermediate ice concentrations is often used to represent the MIZ. This proxy is the region with sea ice concentration (SIC) between 15% and 80% and is readily available from passive microwave satellite estimates (Comiso et al., 1997; Strong & Rigor, 2013; Strong et al., 2017). The Arctic MIZ extent, when defined as the area with 15-80% SIC, may be expanding relative to the retreating pack ice (Aksenov et al., 2017; Rolph et al., 2020), and wave-ice interactions are emerging as a leading control on seasonal sea ice and the future state of the MIZ (Thomson, Ackley, et al., 2018).

We can obtain a basic understanding of wave statistics through bulk wave characteristics, e.g., significant wave height, but full wave spectra contain additional information that becomes critical for frequency-dependent wave-ice interactions. When considering wave spectra in ice, we expect to see a narrowing of the spectral bandwidth as energy is concentrated at the low frequencies indicative of swell (Thomson et al., 2019). This narrowing occurs as waves enter the ice due to dependence of the wave-attenuation rate on frequency, where low-frequency energy is better able to survive compared to high-frequency energy (Wadhams et al., 1988; Meylan et al., 2014; Rogers et al., 2016). We do not have a comprehensive explanation for the physical processes responsible for the dissipation of wave energy in the MIZ (Meylan et al., 2018).

Swell, the low-frequency waves that have traveled outside of their original wind-generation area, can penetrate hundreds of kilometers inside the sea ice edge when the wave heights are large, according to observations from the Antarctic (Kohout et al., 2014; Li et al., 2015) where wave periods can become longer than in the Arctic Ocean. In contrast, high-frequency waves generated by local winds tend to dissipate during their first 10-20 km of travel into the sea ice field, according to Squire and Moore (1980). However, Masson and Leblond (1989) developed a model explaining how local wind waves can be generated in areas of low ice concentration and sparse ice floes. In surface buoy measurements, Smith and Thomson (2016) found support for the open water distance between floes as a control parameter for wave energy. Intense winds acting directly on sea ice, rather than on open water, can drive local wave generation even in Arctic pack ice (Johnson et al., 2021). While these studies have provided a constructive framework for studying ice-affected wind waves, we currently have a limited understanding of the impact and prevalence of locally generated, high-frequency wind waves in sea ice.

The absence thus far of wave-ice interactions in coupled climate models may explain some of the differences in Arctic sea ice between models and observations reported by several studies (e.g., Shu et al., 2020; Notz & Community, 2020). Tietsche et al. (2014) found that model errors in sea ice concentration are most severe in the MIZ, and Blanchard-Wrigglesworth et al. (2021) hypothesize that ocean waves may be responsible for the greater high-frequency variability in sea ice extent found in observations compared to CMIP models, which do not simulate wave-ice interactions.

Despite persistent uncertainty in wave-ice modeling (Meylan & Squire, 1994; Squire, 2007; R. Wang & Shen, 2010; Collins & Rogers, 2017; Squire, 2018; Shen, 2019; Voermans et al., 2019), recent years have seen major advances in the development of fully coupled wave-ice models (Williams et al., 2013; Horvat & Tziperman, 2015; Roach, Horvat, et al., 2018; Roach et al., 2019; Boutin et al., 2018, 2020; Aksenov et al., 2020). Roach, Horvat, et al. (2018) and Roach et al. (2019) incorporated a prognostic sea ice floe size distribution (FSD) in a global sea ice model coupled with an ocean surface wave model, representing wave-ice interactions in both the Arctic and Antarctic for the first time. This model includes a physical relationship between floe fracture, lateral melt potential, and ice-albedo feedback. In contrast to other approaches, the model also includes dependence of wave attenuation on floe size (Meylan & Squire, 1994; Montiel et al., 2016; Meylan et al., 2021). The Roach et al. (2019) model is a focus of this paper and is described further in section 2.1.

The scarcity of observations of waves in ice continues to be an obstacle for both model evaluation and theoretical understanding. Obtaining valid measurements of wave spectra is a challenge when sea ice obscures the ocean surface. The variety of ice conditions, ranging from sparse pancake floes to extensive sheets of ice, complicates interpretation, and existing datasets sample a limited range of ocean and sea ice conditions (Collins et al., 2015). Furthermore, for any fixed location, there is a short window of time during the ice melt and growth seasons when waves in ice can be observed. Remote sensing is a promising path for extending spatial coverage and obtaining more robust wave-ice statistics, and recent efforts have produced estimates of wave heights in the presence of ice using satellite measurements (Ardhuin et al., 2017, 2019; Stopa et al., 2018; Horvat et al., 2020). Nevertheless, basin-scale, long-term observations from remote sensing are not yet available. Multi-year in situ observations, however, are available from three recent field campaigns in the Western Arctic: the Arctic Sea State (Thomson, Ackley, et al., 2018), the Beaufort Gyre Observing System (BGOS), and the Stratified Ocean Dynamics in the Arctic (SODA) programs. These three sets of measurements are a focus of this study and are described further in section 2.2.

Here, we interpret this collection of in situ observations spanning 2012-2019 in the Beaufort Sea from subsurface moorings, supplemented by deployments of freely drifting surface buoys during wave events, measuring ocean surface waves in partial ice cover. We compare the in situ observations with results from the Roach et al. (2019) coupled sea ice-surface wave model forced with atmospheric reanalysis by evaluating wave heights, wave spectra, and the nondimensional scaling relations that can distinguish local wind-generated waves from swell. Global climate models, including the model considered in this study, have errors in ice-edge position that preclude point-by-point comparison with individual observations, so here we aggregate multiple datasets into a relatively large sample to support statistically motivated model evaluation of waves in ice in the Beaufort Sea.

In section 2, we describe the Roach et al. (2019) model and the in situ observations. We relate the methods of model-observation comparison in section 3 and present results of the comparisons in section 4. We discuss the results in section 5 and conclude in section 6.

2 Model and Observations

2.1 Coupled Wave-Ice Model

We analyze results from an experiment using the Los Alamos sea ice model, CICE5 (Hunke et al., 2015) coupled to the ocean surface wave model, Wavewatch III v5.16 (The WAVEWATCH III (R) Development Group (WW3DG), 2016). To simulate wave-ice interactions, the model includes a prognostic FSD developed by Roach, Horvat, et al. (2018) and Roach et al. (2019). Floe sizes are determined by lateral growth and melt, welding of floes in freezing conditions, and the ocean surface wave spectrum through floe fracture and wave-dependent new ice formation. Attenuation of wave spectral energy in ice depends on mean floe size, ice concentration, and ice thickness based on an empirical fit to floe-scattering theory, including a supplemental attenuation term for long wavelengths (Meylan et al., 2021). Figure S1 includes illustrative values of wave attenuation coeffi-

Table 1. Summary of In Situ Observations

Dataset	Instrument	Period	(Lat., Lon.)	0-100 km[1]	100+ km[1]
BGOS-A	AWAC	2012-2018	(75 N, 150 W)	27	68
BGOS-D	AWAC	2013-2018	(74 N, 140 W)	84	4
SODA-A	Signature500	2018-2019	(73 N, 148 W)	39	10
SODA-B	Signature500	2018-2019	(75 N, 146 W)	97	3
SODA-C	Signature500	2018-2019	(78 N, 139 W)	0	19
SWIFTs[2]	Buoy	Oct-Nov 2015	various	838	22
BGOS-SODA Total (excludes SWIFTs)				247	104

[1]Number of valid wave measurements in sample with significant wave height exceeding the 0.3 m detection limit of the BGOS-SODA moorings; data is grouped by distance inside the ice edge (Δ^{dist}; see section 3.1)
[2]Represents 27 buoy deployments

cients for various floe sizes, ice thickness values, and wave periods. Thicker ice tends to cause stronger attenuation, whereas the effect of floe size depends on the period considered. Shorter periods always experience stronger attenuation.

Both the sea ice model and ocean surface wave model evolve freely while forced with JRA-55 atmospheric reanalysis (Kobayashi et al., 2015; Japan Meteorological Agency, Japan, 2013) and coupled to a slab ocean model (SOM) (Bitz et al., 2012). The SOM is a single-layer model, diagnosed from the monthly climatology of a control run of the Community Climate System Model Version 4 (CCSM4), that specifies mixed-layer depths constant in time, annually periodic ocean surface currents, and an annually periodic ocean heat transport convergence, the Q_{flux}; all three SOM input parameters vary in space. The sea ice and wave models are on a displaced-pole nominal 1° grid (gx1v6), and the size of model grid cells near observations in the Beaufort Sea is approximately 50 by 50 km. The simulation spans 1979-2019, and we analyze hourly model output over 2012-2019 in line with the period of observations. The experiment is identical to FSD-WAVEv2 in Roach et al. (2019), except we use a higher coupling frequency between the wave and sea ice components. Here, the wave and sea ice components exchange the ocean surface wave spectrum and sea ice concentration, thickness, and mean floe size every hour to better resolve short-timescale wave-ice interactions.

2.2 In Situ Observations

By aggregating sources of observations that span multiple years with generally continuous sampling, we compile a relatively large dataset to support statistical model evaluation. This dataset, denoted henceforth as BGOS-SODA, consists of two groups of subsurface moorings, spanning 2012-2019 and five locations in the central Beaufort Sea (Table 1; Figure 1). In this section, we briefly review each source of observations.

The first group included in the BGOS-SODA aggregate dataset comes from the Beaufort Gyre Observing System (Krishfield et al., 2014). BGOS includes two subsurface moorings, BGOS-A and BGOS-D, with upward-looking Nortek Acoustic Wave and Current (AWAC) instruments for surface tracking. BGOS-A and BGOS-D sample every hour and began collecting measurements in 2012 and 2013, respectively. Raw data are processed following Herbers et al. (2012), Kuik et al. (1988), and Thomson, Girton, et al. (2018) and converted to wave energy spectra. Data from 2012 is reported in Thomson and Rogers (2014), and a reanalysis of the same data is found in Smith and Thomson (2016). Here, we employ an extended dataset that is mostly continuous from 2012-2018 (Thomson, 2020).

The second group comes from the Stratified Ocean Dynamics in the Arctic project. Three subsurface moorings, denoted SODA-A, SODA-B, and SODA-C, use the upward-looking Nortek Signature Doppler profiler for acoustic surface tracking. Raw data from SODA are quality-controlled using methods comparable to the BGOS methods, producing measurements of surface wave spectra sampled every two hours. Data from the SODA moorings first appear in Brenner et al. (2021), but the wave spectra have not been previously reported. The SODA dataset spans 2018-2019.

Both sets of subsurface moorings detect surface gravity waves via altimeter measurements of surface displacement. An important nuance of the moorings is that the surface tracking simultaneously measures surface gravity waves and sea ice draft. However, the signal from surface waves can be distinguished from that of ice based on spectral characteristics. This separation is part of the quality-control process. Deformed sea ice produces a "red" spectrum with under-ice topography exhibiting peak spectral variance primarily at low frequencies (Rothrock & Thorndike, 1980), whereas the surface gravity waves tend to have peak energy in the frequency range of 0.5 to 0.05 Hz, causing sea surface displacements with distinct spectra in that range. Calm waters and smooth ice both produce flat ("white") spectra. If both ice and waves are present, moorings measure a superposition of both signals.

The processing strategies for the mooring datasets make use of these different spectral shapes to identify and separate wave signals from sea ice. The postprocessed wave datasets from BGOS and SODA exclusively contain observations where the surface gravity wave signal is sufficiently strong to be considered a wave, determined by the spectral shape and the total energy in the frequency range of ocean surface waves. If the ice-draft signal is strong while the surface wave signal is weak, the instrument may be unable to produce a valid wave measurement. These instances where only ice draft is detected are excluded from the wave datasets considered here. The resulting wave dataset almost exclusively contains observations with minimal ice draft detected; when the mooring is in partial ice cover, valid wave measurements appear to come from the water between ice floes.

Separately, we include data from free-drifting surface buoys as a supplemental line of comparison. These measurements come from Surface Wave Instrument Floats with Tracking (SWIFTs) (Thomson, 2012) that were deployed for short periods of time during large wave events in the Oct-Nov 2015 Arctic Sea State campaign. The SWIFTs measure ocean surface velocities and infer wave energy spectra every hour using GPS tracking (Herbers et al., 2012). Because the SWIFTs do not sample data continuously over extended periods of time, we cannot use their results for statistical model evaluation. The surface buoy data from the SWIFTs nonetheless inform interpretation of both the model results and the BGOS-SODA observations.

3 Methods

A primary goal of this study is to objectively compare the in situ observations (located at specific points) and the model results (generalized over a region). We limit the model-observation comparison to the central Beaufort Sea region surrounding the observations: latitudes 72°N to 79°N, longitudes 165°W to 130°W (Figure 1). Ideally, we would focus on model results from the particular grid cells that contain the location of each observation. However, even small errors in the model ice edge position and ice concentration have substantial impacts on where waves occur in the ice, so we cannot expect the coupled model to precisely replicate the observed waves at a given location. Rather, we assess whether the general character of waves in the region is accurately represented in the model.

3.1 Distance Inside the Ice Edge

To generalize the comparison, we group observations and model results based on a calculated distance from the ice edge, denoted as Δ^{dist}. Following convention, the ice edge is defined as the 15% ice concentration contour, roughly separating partial ice cover from open water. Δ^{dist} for a given location inside the ice cover is calculated purely from the ice concentration. The calculation is the Haversine distance to the nearest open water location, i.e., an ocean grid cell with SIC less than 15%. We note that the Δ^{dist} metric does not directly represent the distance along which wave attenuation occurs. The distance into the ice that a wave will travel before full dissipation depends on its direction of propagation, whereas this grouping by Δ^{dist} rather distinguishes locations based on their separation from open ocean. For simplicity, we show three Δ^{dist} groups: open water (SIC $<$ 15%), 0-100 km inside the ice edge (equivalent to approximately two 50x50 km grid cells), and 100+ km inside the ice edge. We choose to group the data based on Δ^{dist} for three reasons:

1. Waves attenuate exponentially with distance as they enter ice cover (Squire & Moore, 1980; Wadhams et al., 1988; Meylan et al., 2018).
2. Groupings based on Δ^{dist} reduce dependence on replicating the true ice-edge position in the model; this enables comparison between locations that are similar in the model and the in situ observations (based on their relative Δ^{dist}), rather than comparison between only the precise locations of the observations.
3. Specific estimates of ice concentration from passive microwave satellite data are highly uncertain in partial ice cover, but identification of the 15% concentration contour has higher confidence based on good agreement with ice-edge positions determined by aircraft (Cavalieri et al., 1991; Fetterer, 2002; Fetterer et al., 2017).

We estimate the time-varying Δ^{dist} for each in situ observation using the NOAA/NSIDC Climate Data Record (CDR) of sea ice concentration, a daily satellite product derived from passive microwave observations (Fetterer et al., 2017). We regrid the satellite estimates from the native 25-km resolution to the model's nominal 1° resolution grid before computing Δ^{dist}, ensuring consistency between the model and observations. This produces a Δ^{dist} for each in situ observation and each model grid cell in the Beaufort Sea at all points in time.

3.2 Nondimensional Scaling for Wind-Generated Ocean Waves

To support interpretation of wave statistics, we employ nondimensional scaling relations for wind-generated waves following Young (1999). These relations enable separation of wind waves from swell and provide an estimate of the implied fetch for observed wind waves in partial ice cover. We calculate the following nondimensional variables for wave energy E, frequency F, and fetch distance X:

$$E = \left(\frac{gH_s}{4U_{10}^2}\right)^2, \qquad F = \frac{f_p U_{10}}{g}, \qquad X = \frac{gx}{U_{10}^2}, \tag{1}$$

where g is the gravitational acceleration; U_{10} is the 10-meter wind speed at the location of each in situ observation and model grid cell from JRA-55 reanalysis; H_s is the significant wave height, defined as 4σ where σ^2 is the variance of the sea-surface height; f_p is the peak frequency; and x is the fetch, i.e., the distance over which waves are generated by local winds. H_s and f_p are measured in situ and provided in model output. The fetch x is not measured but rather inferred for specific wind waves as described below; we refer to this variable as the implied fetch.

In the marginal sea region of the observations considered, wave generation is generally limited by fetch rather than wind duration (Hasselmann et al., 1973; Thomson & Rogers, 2014). Several studies have developed empirical estimates of power laws for E

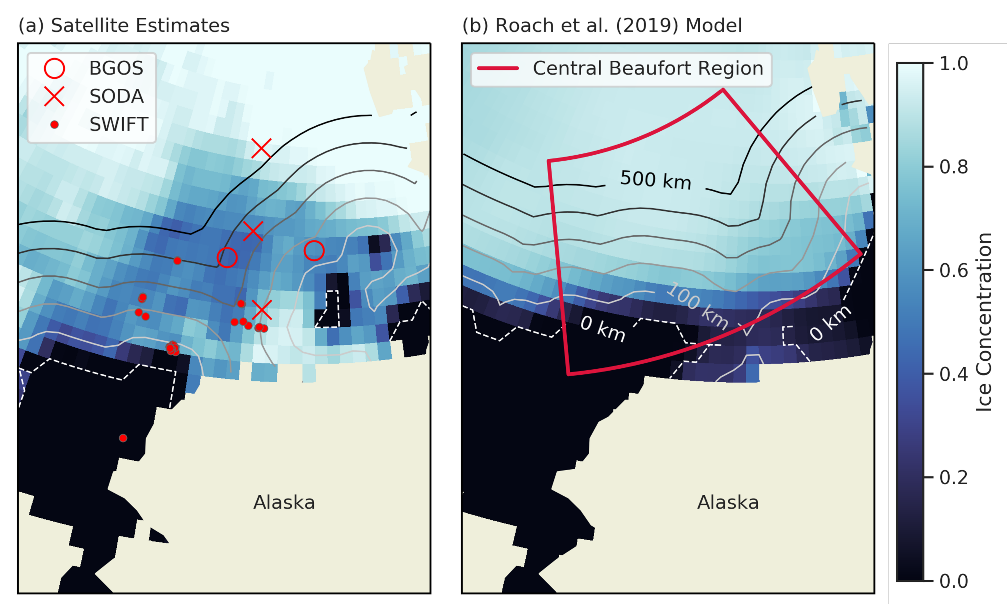

Figure 1. Sea ice concentration (color shading) and corresponding Δ^{dist} (contour lines every 100 km from 0-500 km) at a sample, illustrative date (23 July 2018). (a) Satellite estimates of concentration with locations of in situ observations (red symbols). (b) Results from Roach et al. (2019) model with region used for comparison with observations (red box). Note that the 0-km-distance contour simultaneously denotes 15% ice concentration.

vs. X and F vs. X that describe wind-generated waves in a fetch-limited regime. Young (1999) combined these estimates into the relations

$$E = (7.5 \pm 2.0) \times 10^{-7} X^{0.8} \tag{2}$$

$$F = (2.0 \pm 0.3)\, X^{-0.25}, \tag{3}$$

which apply at least until reaching a fully developed limit for pure wind seas at $E_{max} = (3.6 \pm 0.9) \times 10^{-3}$ and $F_{min} = 0.13 \pm 0.02$. Using equation (1), we reformulate these power laws in terms of the variables available from measurements and modeling, E and F:

$$E = (6.9 \pm 3.8) \times 10^{-6} F^{-3.2}. \tag{4}$$

We identify waves that are accurately described by fetch-limited local wind generation, i.e., wind waves, as those that fall within the uncertainty bounds of the line defined by the power law in equation (4). If a spectrum has less energy E than predicted by the wind-wave power law for a given frequency F, and it has a wave age greater than 1, we determine that the spectrum represents swell, i.e., long-period waves produced by nonlocal winds.

Wave age $\frac{c}{U}$ is a nondimensional parameter defined by the ratio of the dominant phase speed c_p to the wind speed U_{10}, where we treat $c_p = \frac{g}{2\pi f_p}$ following the deep-water limit for surface gravity waves. When the wave age exceeds 1, waves travel faster than the winds. We note that wave age can be expressed in terms of F using equation (1) such that $\frac{c}{U} = (2\pi F)^{-1}$, and wave age is greater than 1 when F is less than $\frac{1}{2\pi}$.

Taking only the spectra that appear to be fetch-limited local wind waves, based on equation (4) and wave age as described above, we can calculate an implied fetch x

corresponding to each wind-wave spectrum. This dimensional variable x is recovered by solving for the nondimensional X in equation (2) based on the known energy E, then using equation (1) to restore the dimension. The implied fetch is an estimate of the open water distance that would be required for local winds to generate a given wind-wave spectrum.

4 Results

4.1 Significant Wave Height

We compare the significant wave height H_s statistics by aggregating observations from the five BGOS and SODA moorings into a single dataset. Figure 2 shows the combined BGOS-SODA wave height distributions in open water (SIC $<$ 15%), 0-100 km Δ^{dist}, and $\Delta^{\text{dist}} > 100$ km. The lower bound for H_s is set at 0.3 m for the aggregate dataset to account for detection limits that vary across instruments. Model results are similarly represented as a histogram by aggregating the 2012-2019 statistics from each grid cell in the Beaufort Sea region surrounding the observations.

The H_s distributions have similar shapes in open water (Figure 2a), but the model has more frequent large waves, with 18% of H_s greater than 2.0 m compared to 9% in observations. The observations show slightly greater probability for smaller waves between 0.5 and 1.0 m. We note that sampling bias likely influences the open water comparison given that we do not control for distance outside the ice edge, i.e., all open water results are in a single group. A detailed analysis of open water results, however, is outside the scope of this study.

We find more notable differences between the distributions in partial ice. The 0-100 km group (Figure 2b) displays a strong contrast, where the model's distribution is dominated by the smallest waves near the lower-limit of the domain, while observations show a higher prevalence of large waves. The model has only 13% of H_s greater than 1.0 m, whereas 35% of observations exceed 1.0 m.

The 100+ km Δ^{dist} distributions differ most strongly in terms of kurtosis (Figure 2c). The model has a prominent peak at the smallest end of wave heights, paired with a thicker tail of large waves. 9% of the model's H_s exceed 1.0 m, whereas the 104 observations at 100+ km do not report any H_s beyond that magnitude. Only 5% of observed H_s exceed 0.75 m, and the distribution is relatively uniform between 0.30 and 0.75 m. We discuss how sampling biases could affect this model-observation comparison in discussion section 5.2 below, but we emphasize here that the absence of H_s beyond 1.0 m in BGOS-SODA observations cannot be attributed to instrument errors. Such large wave heights exceed minimum wave height detection limits by significant margins and are reported in open water and at 0-100 km Δ^{dist}. The absence of H_s greater than 1.0 m in the BGOS-SODA observations of Figure 2c is a robust result within the limit of our sample size. To provide some insight on differences in the distributions, we turn to the spectra.

4.2 Wave Spectra

Even if the bulk wave parameter H_s appears accurately represented, the model can have significant biases in how wave energy is distributed between low and high frequencies. Inspecting the full wave spectra reveals that similar H_s may have dramatically different signatures in frequency space, and these model-observations differences can highlight disagreement in wave attenuation and generation processes. Additionally, we introduce spectra from the SWIFT surface buoys as a supplemental line of comparison, recalling that SWIFTs preferentially sample significant wave events as part of experiment design.

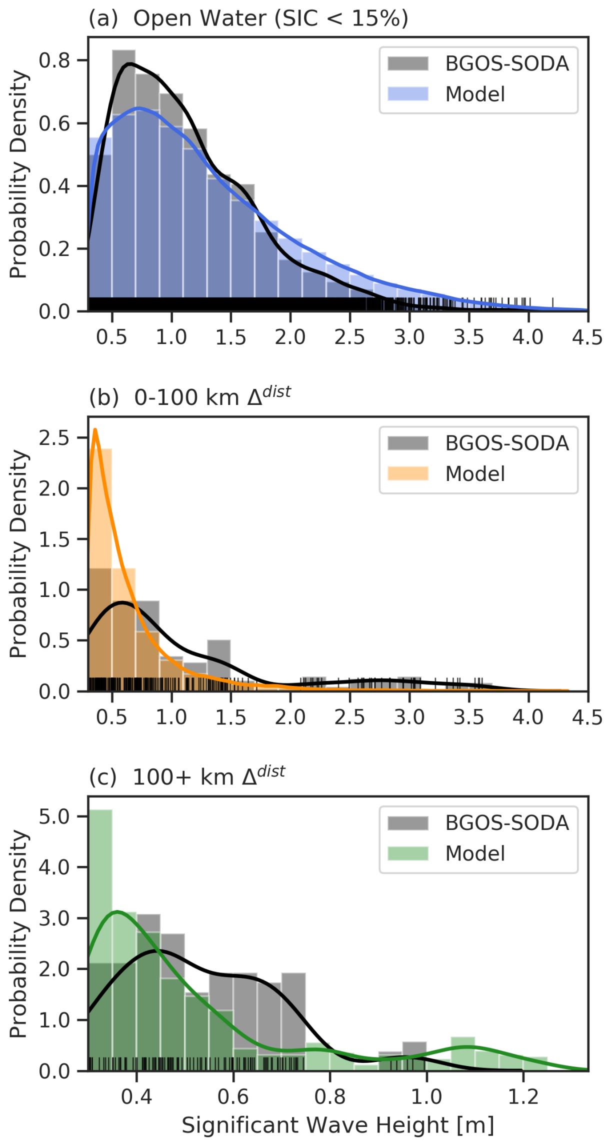

Figure 2. Histograms and density curves for significant wave height H_s distributions in (a) open water (sea ice concentration $< 15\%$), (b) 0-100 km Δ^{dist}, and (c) 100+ km Δ^{dist}, spanning 2012-2019 in the Beaufort Sea. In situ observations (black) are aggregated from two BGOS and three SODA moorings, and rug plots of vertical black lines along the x-axes denote exact values of individual observations. Model results (colors) are from the Roach et al. (2019) model, restricted to the Beaufort region surrounding observations. The lower bound on the domain for H_s is set at 0.3 m, limiting the results to those exceeding the detection limit for all moorings considered. Note the different x-axis scale in panel (c).

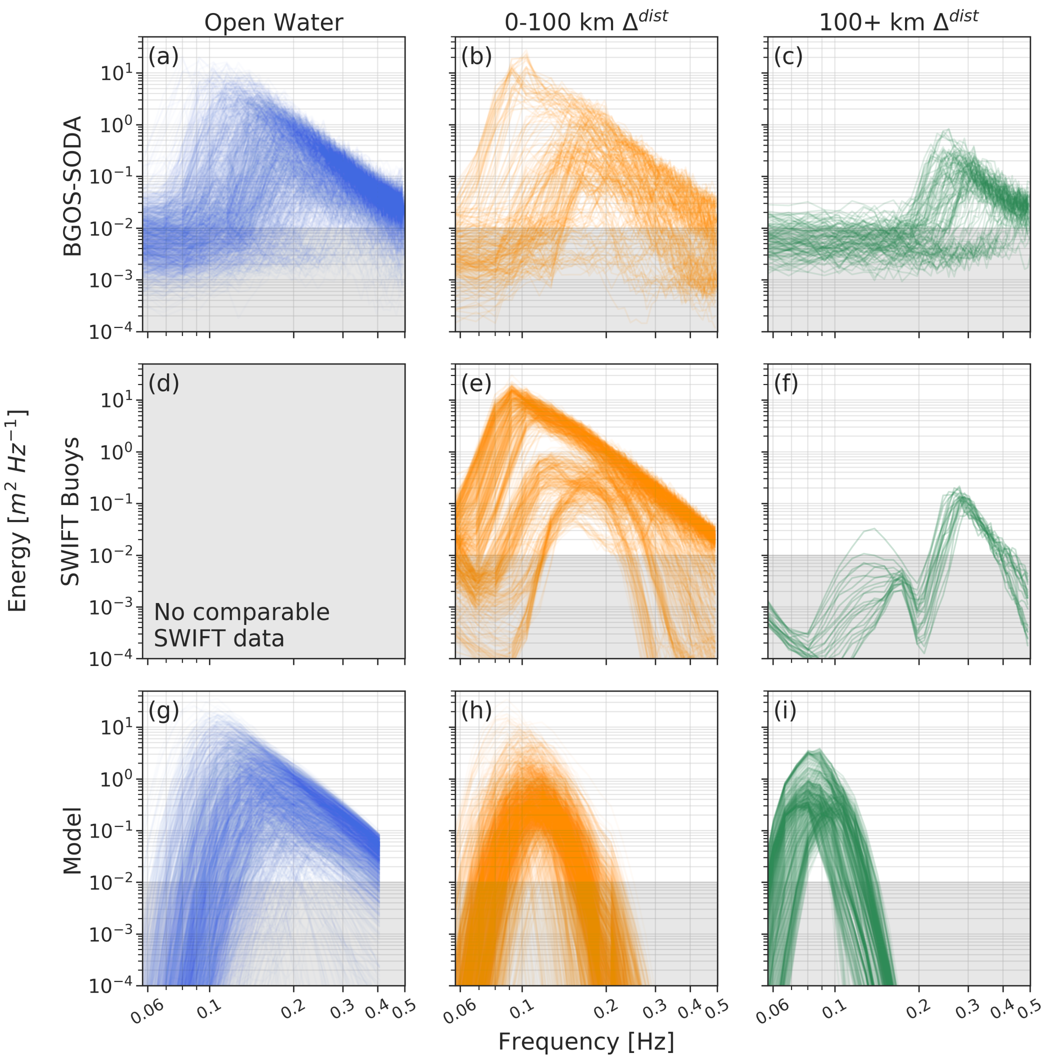

Figure 3. Ocean surface wave spectra grouped by distance inside the ice edge (Δ^{dist}). Top row (a)-(c): BGOS-SODA mooring observations. Middle row (d)-(f): SWIFT surface buoys. Bottom row (g)-(i): Roach et al. (2019) model results from grid cells in central Beaufort region surrounding observations. Open water (SIC < 15%) in left column, 0-100 km Δ^{dist} in center column, and 100+ km Δ^{dist} in right column. Only spectra with H_s greater than 0.3 m are shown. Gray shading represents the approximate BGOS-SODA detection limit and is included on all panels for ease of comparison.

The open water (SIC < 15%) spectra are generally in agreement between the moorings and the model (Figure 3a,g). We can identify the prominent spectral shape of locally developed wind waves in open water in both panels. These spectra exemplify a characteristic power-law relationship between energy and frequency (different from the nondimensional-scaling power law described in section 3.2) in the high-frequency spectral tail, i.e., the portion of the spectrum where frequency f is higher than the peak frequency f_p. In open water, the spectral tail follows a consistent f^{-4} slope down from f_p (Phillips, 1985; Thomson et al., 2013; Lenain & Melville, 2017).

In sea ice, the spectral tail is typically steeper than f^{-4} in observations and model results. This steeper tail has been reported in observations before (Rogers et al., 2016; Thomson et al., 2021) and is consistent with the notion that sea ice dissipates high-frequency energy most effectively. Data from the 0-100 km transition into ice, illustrated most clearly by the fan of spectral tails in the SWIFT spectra (Figure 3e) but also visible in the moorings (Figure 3b), demonstrates that waves undergo a frequency-dependent attenuation while traveling through partial ice and preferentially lose energy at the highest frequencies. The model does not show the same spread of spectral-tail slopes seen in observations, even in the first 0-100 km of partial ice (Figure 3h); all energy at high frequencies has been eliminated. A spectral shape similar to the model results, however, can be seen in some observed spectra at 0-100 km (Figure 3b,e), albeit shifted so that f_p tends to be at slightly higher frequencies in observations.

Moving to 100+ km Δ^{dist}, we see a structural difference between the spectra in the model and those in the observations. In Figure 3i, the model shows waves retaining significant low-frequency energy far into the ice, and all of these model spectra are devoid of any high-frequency energy. On the other hand, the BGOS-SODA observations (Figure 3c) have a spectral signature that is, perhaps surprisingly, reminiscent of a short-wave subset of the open water spectra. These spectral tails follow the f^{-4} slope, and all energy is at relatively high frequencies. The contrast between the model's low-frequency energy and the BGOS-SODA high-frequency waves suggests that there are two separate modes displayed in the spectra at 100+ km Δ^{dist}. The SWIFTs in Figure 3f show bimodal spectra that appear to have a swell wave group at lower frequencies concurrent with a local-wind-wave group at higher frequencies. Notably, the swell group in these bimodal spectra has higher f_p and less energy compared to the model results in Figure 3i, and energy is mostly below the BGOS-SODA detection limit.

4.3 Fetch Scaling

We find that the distinction between swell and wind waves generally can be reduced to the nondimensional scaling of two bulk wave parameters, H_s and f_p, rather than requiring inspection of the full spectra. Whereas the H_s distributions in Figure 2 compare amounts of wave energy, the distributions in Figure 4 compare how the swell and wind-wave modes are represented. Figure 4 applies the nondimensional scaling relations between energy and peak frequency to observations and the model, and it also includes the power law for local wind-wave generation (see section 3.2). The points that follow the power law are identified as locally generated wind waves, while points located below the line, i.e., those with less energy than predicted by the power law for a given peak frequency, and with wave age greater than 1 are identified as swell. These modes are not always well-separated because nonlocal swell and local wave generation can co-occur.

The power law captures most of the open water (Figure 4a) observations and model output, but a nonlocal component can be identified in both the model and observations that pulls some of the points below the power-law line and towards low F such that the wave age is greater than 1. This consistency between the model and observations suggests that there is not a significant bias in the prevailing wave modes in open water.

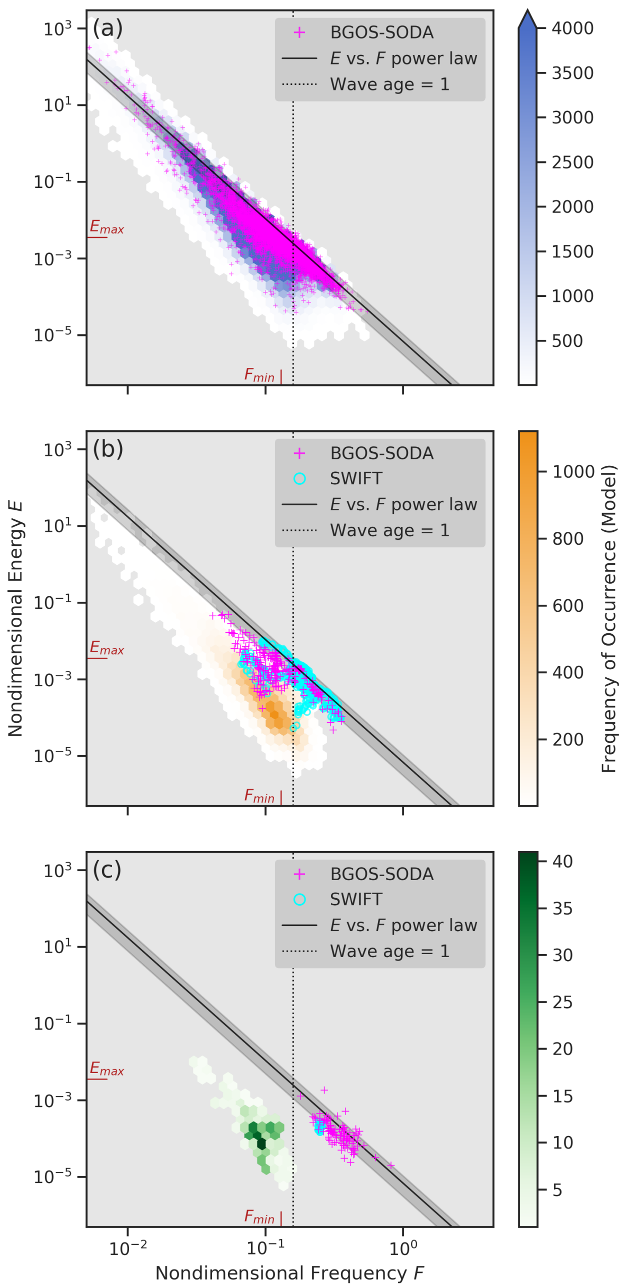

Figure 4. Nondimensional scaling of wave energy vs. peak frequency grouped by distance inside the ice edge (Δ^{dist}). Observations shown as scatter plots (BGOS and SODA moorings as + symbols; SWIFT surface buoys as O symbols). Roach et al. (2019) model results from central Beaufort region surrounding observations shown as 2-d histograms (color shading), where the hourly mean at each model grid cell is a separate data point. (a) Open water (SIC < 15%), (b) 0-100 km Δ^{dist}, and (c) 100+ km Δ^{dist}. Only results with $H_s > 0.3$ m are shown. Power law (black line) with confidence intervals (shading) of E vs. F for wind-generated, fetch-limited waves, with the fully developed limit (E_{max} and F_{min}) for pure wind seas denoted in red (Young, 1999). Dashed line at $F = (2\pi)^{-1}$ indicates wave age = 1; where $F < (2\pi)^{-1}$, wave age > 1.

In partial ice, the results for the model become distinct from the observations. At 0-100 km Δ^{dist} (Figure 4b), the model immediately clusters at lower energies away from the power law, i.e, the swell mode dominates. In observations at 0-100 km, we see a spread both on and off the power-law relation. Recall that this spread, due to the combined presence of swell, local wind waves, and attenuation by the ice cover, can be seen in the mooring and SWIFT spectra (Figures 3b,e).

At 100+ km Δ^{dist}, separation between the model and the observations is most definite (Figure 4c). The model displays only the swell mode of lower energies with wave age greater than 1 and is removed from the wind-wave power law even more strongly than in the 0-100 km zone. The observations behave differently; they do not continue spreading away from the power law toward lower energies as seen in their 0-100 km subset. Instead, they return to clustering along the power law, indicating local wind-wave generation at 100+ km Δ^{dist}. The observations thus suggest that local wave generation is a significant source of wave activity far within the marginal ice zone, and this source is not captured in the model.

5 Discussion

While the coupled wave-ice model of Roach et al. (2019) broadly captures the range of significant wave heights in BGOS-SODA observations, comparing the shapes of the H_s distributions suggests there may be substantial differences which are not apparent when considering the bulk parameter for wave energy alone. The spectral details are important given the frequency dependence of wave attenuation and floe fracture. Two key questions emerge from the spectra and nondimensional scaling at 100+ km Δ^{dist}: why do BGOS-SODA observations show wind waves but no swell, and why does the model show swell but no wind waves?

5.1 Wind Waves

Sea ice is known to filter out high-frequency wave energy, but BGOS-SODA observations nevertheless reveal a prevalence of high-frequency wind waves at 100+ km Δ^{dist} (Figure 4c). A possible explanation is that local generation of wind waves, perhaps in leads or the open water areas between sparse ice floes, occurs at significant distances inside the MIZ. In Figure 5, we calculate the implied fetch for each wind-wave spectrum in BGOS-SODA observations according to the scaling relations (as described in section 3.2). All observed wind waves at 100+ km Δ^{dist} could be generated by winds blowing over open water distances estimated to be less than 50 km.

Wind waves in ice are absent in model results for the central Beaufort due to multiple potential factors. First, the short implied fetch of the observed wind waves reveals that they are a sub-grid-scale process. The distance across the model grid cells, which are approximately 50 by 50 km in this region, is longer than the implied fetch for all observed wind waves at 100+ km Δ^{dist} (Figure 5). These short waves are sensitive to model parameters that control sub-grid-scale wave generation in partial ice.

Additionally, the model is biased high for intermediate ice concentrations (Figure 6), i.e., the 15-80% concentration range, at 100+ km Δ^{dist} during the summer melt season when wind waves in ice occur in observations (Figure S2). We focus on bias in the 15-80% intermediate concentration range conventionally considered part of the MIZ. We exclude compact pack ice (SIC > 80%) because the large number of compact pack ice grid cells dominates the distribution. For the intermediate-concentration subset of grid cells, satellite estimates indicate a greater proportion of low ice concentrations compared to the model (also see Figure 1 for an illustrative example). Because wind-wave generation in Wavewatch III is scaled by a coefficient equal to the local open water fraction, the bias toward high ice concentrations excessively inhibits local wave generation at 100+

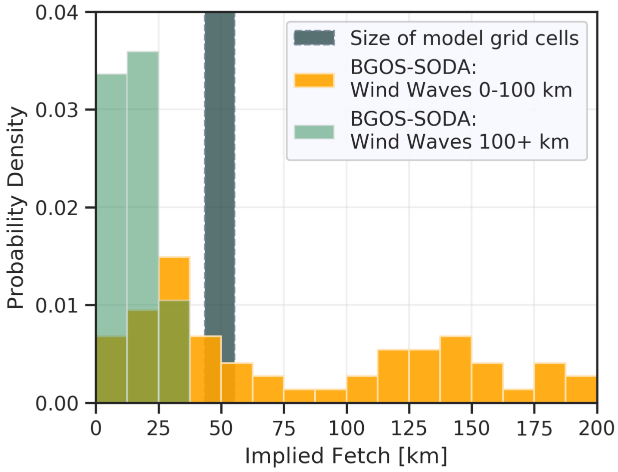

Figure 5. Histograms of implied fetch for locally generated wind waves from BGOS and SODA mooring observations. Observations located 0-100 km Δ^{dist} (orange) and 100+ km Δ^{dist} (green). Size range of Roach et al. (2019) model grid cells (approximately 50x50 km) in the vicinity of observations shown as dark shading with dashed border.

km Δ^{dist}. We note that the lack of local wave generation could be partially responsible for the high concentration bias, just as the high concentrations are potentially responsible for suppressing wave generation.

Wind bias in the model could also be partially responsible. However, model winds come from atmospheric reanalysis. We believe error in the reanalysis is not a likely explanation, although we note that reanalysis does not always capture wind events in the MIZ (e.g., Brenner et al., 2020).

Are these high-frequency wind waves important for modeling wave-ice interactions? In the Roach et al. (2019) model, waves can impact the FSD via floe fracture, described using the sub-grid-scale parameterization developed by Horvat and Tziperman (2015). To test the importance of the observed high-frequency wind waves for floe fracture, we input the median, 75$^{\mathrm{th}}$ percentile, and maximum wave spectra, ranked by H_s, from BGOS-SODA observations at 100+ km Δ^{dist} to the Horvat and Tziperman (2015) parameterization (computed offline). This parameterization generates realizations of the sea surface height using the ocean surface wave spectrum and computes the strain applied to sea ice floes. A statistical distribution of resulting fractured floe sizes is constructed by computing the distances where the strain field exceeds a critical value. Figure 7a shows the resulting floe size distributions that would be formed by the observed wave spectra in Figure 7c with a representative ice thickness of 0.5 m.

These results suggest that the locally generated waves at 100+ km Δ^{dist} tend to be strong enough to fracture sea ice: the median H_s spectrum reduces 71% of the ice area to floes with radius less than 15 m. Steele (1992) found that, for floes with radius less than 15 m, lateral melt plays a critical role in Arctic summer conditions, which is when these waves appear in observations (Figure S2). Smaller floes make the dominant contribution to cumulative floe perimeter, so short wind waves in ice appear to enhance the lateral melt potential of ice floes and should be a priority for future wave-ice model development.

Note that we cannot expect model spectra to be identical to the observed spectra in partial ice because the model also represents all of the surface area where waves are

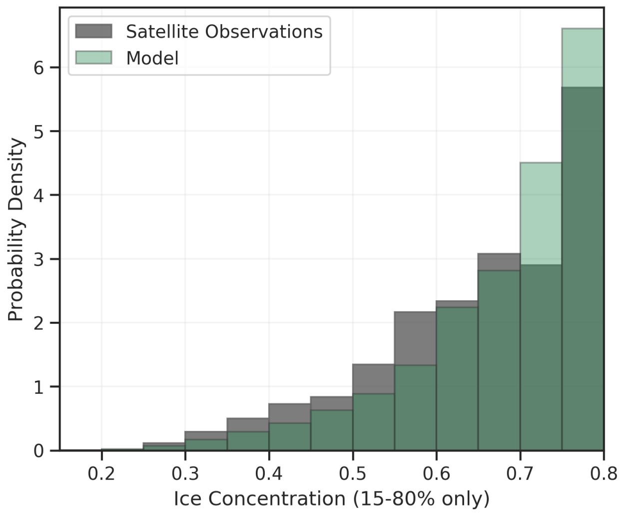

Figure 6. Histograms of intermediate (15-80%) sea ice concentrations during summer melt season (Jun-Jul-Aug) for grid cells located 100+ km Δ^{dist}, spanning 2012-2019 in the central Beaufort region surrounding the in situ observations. Satellite estimates (black) are from the NOAA/NSIDC Climate Data Record, and model results (green) are from the Roach et al. (2019) model.

damped by ice floes. A model grid cell aims to capture mean wave statistics over a partial ice region, but the in situ observations shown here appear to capture wave spectra from open water points between floes (see section 2.2 and the discussion that follows in section 5.2). We speculate that reconciling the model-observations difference in high-frequency energy does not require that model spectra become identical to those from the BGOS-SODA observations at 100+ km Δ^{dist}. However, the complete absence of high-frequency energy in the model spectra is striking and demands attention.

5.2 Swell

Now, we will address why BGOS-SODA observations do not show any swell at 100+ km Δ^{dist} while the model does. Generally, the low-frequency energy of swell experiences less dissipation than high-frequency energy during travel through partial ice cover. We anticipated that observations far inside the ice edge would preferentially show wave energy at low frequencies, similar to what we see in the model results. While large swells are relatively rare, for now, in the central Beaufort even in open water (Thomson & Rogers, 2014), the absence of low-frequency energy in BGOS-SODA observations from 100+ km Δ^{dist}, given its presence at 0-100 km, is conspicuous. In this section, we first consider why BGOS-SODA might not show any swell at 100+ km Δ^{dist}.

Could the BGOS-SODA data processing exclude swell spectra because those spectra also have a sea ice signal from under-ice topography? Recall that the subsurface BGOS-SODA measurements can represent a superposition of both ocean surface waves and sea ice draft, which each have distinct spectral shapes (see section 2.2). When sea ice is present above the moorings, the processing of the altimeter-based measurements may fail to recognize waves due to the additional signal from the ice. Therefore, the lack of swell spectra with H_s greater than 0.3 m at 100 km+ Δ^{dist} in the BGOS-SODA observations could be partly a result of sampling bias if the swell is always coincident with a strong signal from ice. We first test this possibility by manually inspecting individual spectra in the original SODA records. We are able to find some measurements that have been excluded

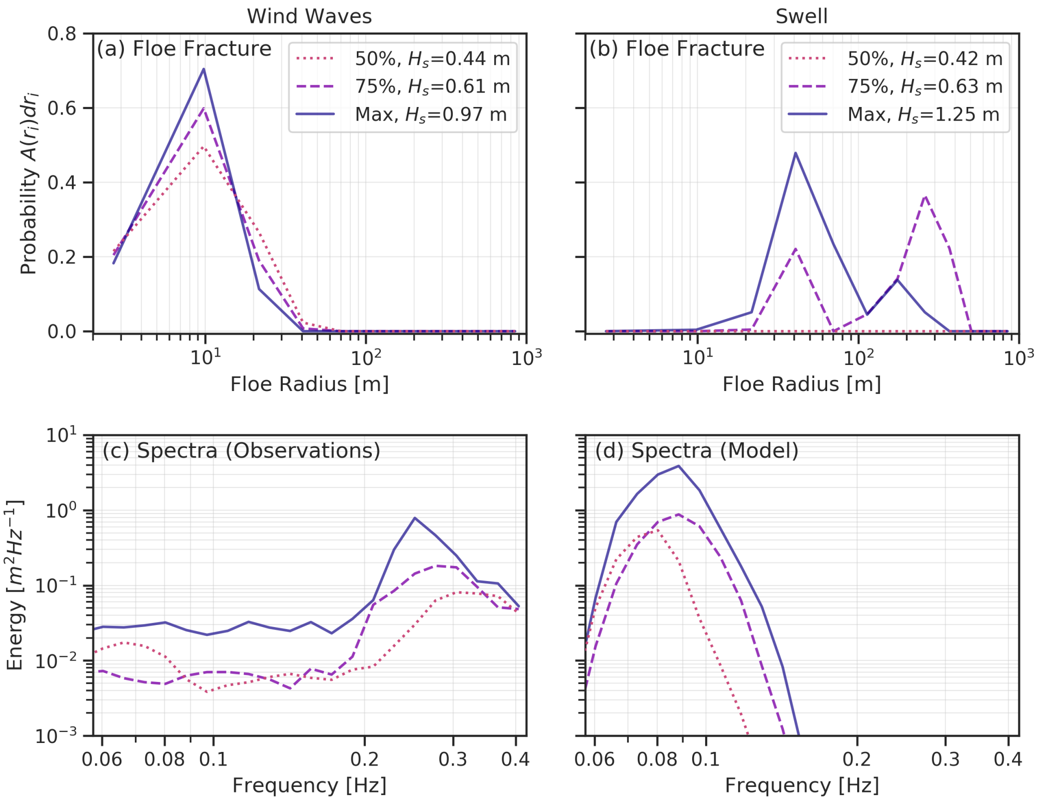

Figure 7. (a)-(b) Histograms of predicted floe-size distributions resulting from corresponding wave spectra in (c)-(d), respectively, present at 100+ km Δ^{dist}, based on the Horvat and Tziperman (2015) parametrization and assuming ice thickness of 0.5 m. Floe sizes in (a)-(b) are binned into probability distributions $A(r)$ where $A(r)dr$ is the fraction of ice area with floe radius between r and $r + dr$. Plots show the probability $A(r_i)dr_i$ at each of the following bin centers i: 3, 10, 22, 41, 70, 114, 176, 260, 370, 506, 668, and 850 m. Wave spectra represent the approximate median (50$^{\text{th}}$ percentile), 75$^{\text{th}}$ percentile, and maximum based on H_s from (c) wind waves in BGOS-SODA observations and (d) swell in the Roach et al. (2019) model results, excluding spectra with H_s less than 0.3 m. Spectra in (c) have been interpolated to the frequency domain resolved in the Roach et al. (2019) model. Note that the 50$^{\text{th}}$ percentile swell spectra in (d) does not cause any floe fracture and appears as a zero line in (b).

by data processing from the wave dataset considered in this study and which have spectral shapes suggesting a combination of both sea ice and swell. However, the H_s of the apparent swell in these spectra are less than 0.3 m, and the waves generally occur outside of the 100+ km Δ^{dist} range. While this manual inspection method is not exhaustive, it suggests there are no pervasive issues in the processing causing swell to be omitted from the data.

Could some swell be entirely hidden by the sea ice signal? If this were the case, the swell signal would be so much weaker relative to the ice signal that it would not emerge from underneath the ice's red spectrum, i.e., the swell would have no detectable spectral signature. Reprocessing of all individual spectra (including when no waves are apparent) allows us to set an upper bound on the H_s of swell that may be hidden from observation based on the spectrum that is measured, which also includes the ice signal. The upper bound is determined by integrating the spectra over a frequency band associated with swell; the true H_s of any hidden swell in this band must be much less than the apparent H_s, i.e., the upper bound, due to how the swell spectral shape compares to a measured red spectrum. If we choose a narrow swell band of 0.08-0.125 Hz based on the peak frequencies of swell in the model results, we find that 6% of the 10,283 SODA measurements that appear to be ice spectra exceed an H_s upper bound of 0.3 m, corresponding to the minimum H_s used throughout the analysis. It is possible that some nontrivial swell could exist hidden in these ice spectra, but we do not find any further evidence of swell with H_s greater than 0.3 m in this band.

We also note that the absence of swell at 100+ km Δ^{dist} is supported by spectra constructed from the moorings' pressure data (not shown). These represent independent estimates of wave signals using a separate instrument on the moorings. The pressure spectra from under ice also do not report H_s greater than the 0.3 m cutoff. A noteworthy supporting example comes from the 11 Oct 2015 event analyzed in Thomson et al. (2019) (see their Figure 2), which shows a swell spectrum from BGOS-A pressure data while the mooring was under ice near a major storm. In that case, the BGOS-A H_s is less than 0.1 m.

We conclude that the 100+ km Δ^{dist} BGOS-SODA observations do not display any swell spectra because any swell that reached the moorings must have been too small to emerge with a sufficient signal. Perhaps the swell that evaded detection by the moorings resembles the swell (lower frequency) wave group in the bimodal SWIFT spectra (Figure 3f), which has energy mostly below the moorings' detection limits. Based on the recent wave climate near these moorings, large swells penetrating beyond 100 km Δ^{dist} in the Beaufort Sea are rare enough that they do not appear in this aggregate dataset.

The model output at 100+ km Δ^{dist} (Figures 2c, 3i, 4c) includes a number of waves exceeding the BGOS-SODA detection limit of 0.3 m H_s, with maximum H_s in the model reaching 1.25 m. Given that we do not see any evidence in BGOS-SODA of swells that approach the size of those in the model, this appears to suggest that the model overestimates the persistence of swell in ice, at least in the Beaufort Sea. The model's excess swell could be attributable to an open water bias that lingers as swell enters the ice, rather than the wave attenuation rate. If incident waves have energy at too-low frequencies in open water, the swell could survive at greater distances inside the MIZ. Comparison of the open water peak-frequency distributions, limited to the ice-growth season when swell is most often present in the model at 100+ km Δ^{dist} (Figure S3a), does not indicate any clear model bias toward low peak frequencies. However, there is an apparent bias of larger H_s that could sustain the swell if that bias were present in the subset of waves that propagate into the MIZ. These explanations for the model swell are speculative, and more data is needed to support further investigation.

Finally, we consider whether the excess swell has a significant impact on floe size. Unlike the high-frequency wind waves, which efficiently reduce floes to small sizes, the low-frequency swell has a less drastic effect. We repeat the floe-fracture test from the wind-wave discussion in section 5.1, now for swell from the model spectra at 100+ km Δ^{dist} using the Horvat and Tziperman (2015) parameterization (Figure 7b). This parameterization suggests that even the biased-high swell in the model fractures floes predominantly into large radius categories, with less than 1% of the ice area reduced to floe radius less than 15 m even for the maximum H_s. In the case of the median H_s, the swell does not cause any floe fracture. Moreover, the swell tends to occur in months of freezing conditions while new ice is forming and the ice edge is moving southward rather than melting and retreating (Figure S2). Overestimation of swell in the model is still a concern, but it appears less consequential for floe fracture and ice melt compared to the wind waves.

6 Conclusions

We investigate differences between the Roach et al. (2019) coupled wave-ice model and an aggregated dataset of recent in situ observations of waves in pack ice from the central Beaufort Sea. We group the data and model output by distance inside the ice edge, denoted Δ^{dist}, to enable a statistical comparison. The distributions of significant wave height are similar in open water but have more notable differences in sea ice. The model tends to have smaller H_s than observations in the first 0-100 km of pack ice and greater kurtosis compared to observations beyond 100 km Δ^{dist}.

The wave spectra and nondimensional scaling of energy and frequency illuminate different prevailing modes of waves at 100+ km Δ^{dist} between the model and observations. We find that observations show significant generation of local wind waves during the ice-melt season at 100+ km Δ^{dist}. The model lacks the resolution to generate the high-frequency wind waves that might arise if leads or open water areas between sparse ice floes were resolved explicitly rather than parameterized based on the sea ice concentration within a grid cell, which is the scheme currently implemented in Wavewatch III. These wind waves appear to cause substantial floe fracture and enhance lateral melt potential. Therefore, resolving or improving the parameterization of local wind-wave generation in the MIZ should be considered a priority in future model development.

On the other hand, the swell mode appears only in the model at 100+ km Δ^{dist}, not in the BGOS-SODA observations. Low-frequency energy appears to be overstated in the model at 100+ km Δ^{dist}. This swell in the model appears predominantly during the ice-growth season and has a relatively minor impact on floe fracture and melt potential compared to the wind waves.

The comparisons with observations in this study reveal important areas of development for modeling interactions between waves and sea ice. Combining multiple wave datasets to form a relatively large sample is an effective approach for model evaluation and could be replicated in other regions. However, we need more robust observations of wave spectra in sea ice across seasons at basin scale. These observations would enable stronger constraints on the physics of wave attenuation and generation in the MIZ which are critical to model development and theoretical understanding.

Acknowledgments

BGOS data were collected and made available by the Beaufort Gyre Exploration Program based at the Woods Hole Oceanographic Institution (https://www2.whoi.edu/site/beaufortgyre/) in collaboration with researchers from Fisheries and Oceans Canada at the Institute of Ocean Sciences, and the BGOS datasets used in this study are available at digital.lib.washington.edu/researchwork SWIFT buoy data were collected and made available by the Arctic Sea State program and can be found at www.apl.uw.edu/swift. SODA data is available at digital.lib.washington.edu/researchworks/h NOAA/NSIDC Climate Data Record estimates of sea ice concentration from passive microwave satellite observations are available at nsidc.org/data/G02202. Model output used in this study is publicly available via Zenodo at https://doi.org/10.5281/zenodo.5545098. V. T. Cooper thanks the United States of America Department of Defense and Office of Naval Research (ONR) for funding support through a National Defense Science & Engineering Graduate (NDSEG) Fellowship. V. T. Cooper, L. A. Roach, and C. M. Bitz were supported by the USA National Science Foundation (NSF) grant OPP-1643431, and L. A. Roach was supported by the New Zealand Ministry of Business, Innovation and Employment under Science Investment Contract C01X1914. J. Thomson was supported by ONR grant N00014-16-1-2349. S. D. Brenner was supported by ONR grant N00014-18-1-2687. M. M. Smith was supported by NSF OPP-1724467 and OPP-1724748. V. T. Cooper thanks Mark Orzech, W. Erick Rogers, and David Bailey for insightful discussions and Luc Rainville for SAR knowledge that contributed to understanding results in this study.

References

Aksenov, Y., Bateson, A. W., Feltham, D. L., Schröder, D., Hosekova, L., & Ridley, J. K. (2020). Impact of sea ice floe size distribution on seasonal fragmentation and melt of Arctic sea ice. *Cryosphere*, *14*(2). doi: 10.5194/tc-14-403-2020

Aksenov, Y., Popova, E. E., Yool, A., Nurser, A. J., Williams, T. D., Bertino, L., & Bergh, J. (2017). On the future navigability of Arctic sea routes: High-resolution projections of the Arctic Ocean and sea ice. *Marine Policy*, *75*. doi: 10.1016/j.marpol.2015.12.027

Ardhuin, F., Stopa, J., Chapron, B., Collard, F., Smith, M., Thomson, J., … Wadhams, P. (2017). Measuring ocean waves in sea ice using SAR imagery: A quasi-deterministic approach evaluated with Sentinel-1 and in situ data. *Remote Sensing of Environment*, *189*. doi: 10.1016/j.rse.2016.11.024

Ardhuin, F., Stopa, J. E., Chapron, B., Collard, F., Husson, R., Jensen, R. E., … Young, I. (2019). *Observing sea states* (Vol. 6) (No. APR). doi: 10.3389/fmars.2019.00124

Asplin, M. G., Galley, R., Barber, D. G., & Prinsenberg, S. (2012, 6). Fracture of summer perennial sea ice by ocean swell as a result of Arctic storms. *Journal of Geophysical Research: Oceans*, *117*(6), 6025. Retrieved from `https://agupubs.onlinelibrary.wiley.com/doi/full/10.1029/2011JC007221https://agupubs.onlinelibrary.wiley.com/doi/abs/10.1029/2011JC007221https://agupubs.onlinelibrary.wiley.com/doi/10.1029/2011JC007221` doi: 10.1029/2011JC007221

Asplin, M. G., Scharien, R., Else, B., Howell, S., Barber, D. G., Papakyriakou, T., & Prinsenberg, S. (2014). Implications of fractured Arctic perennial ice cover on thermodynamic and dynamic sea ice processes. *Journal of Geophysical Research: Oceans*, *119*(4). doi: 10.1002/2013JC009557

Bitz, C. M., Shell, K. M., Gent, P. R., Bailey, D. A., Danabasoglu, G., Armour, K. C., … Kiehl, J. T. (2012). Climate sensitivity of the community climate system model, version 4. *Journal of Climate*, *25*(9). doi: 10.1175/JCLI-D-11-00290.1

Blanchard-Wrigglesworth, E., Donohoe, A., Roach, L. A., DuVivier, A., & Bitz, C. M. (2021, 7). High-Frequency Sea Ice Variability in Observations and Models. *Geophysical Research Letters*, *48*(14). Retrieved from `https://onlinelibrary.wiley.com/doi/10.1029/2020GL092356` doi: 10.1029/2020GL092356

Boutin, G., Ardhuin, F., Dumont, D., Sévigny, C., Girard-Ardhuin, F., & Accensi, M. (2018). Floe Size Effect on Wave-Ice Interactions: Possible Effects, Implementation in Wave Model, and Evaluation. *Journal of Geophysical Research: Oceans*, *123*(7). doi: 10.1029/2017JC013622

Boutin, G., Lique, C., Ardhuin, F., Rousset, C., Talandier, C., Accensi, M., &

Girard-Ardhuin, F. (2020). Towards a coupled model to investigate wave-sea ice interactions in the Arctic marginal ice zone. *Cryosphere*. doi: 10.5194/tc-14-709-2020

Brenner, S., Rainville, L., Thomson, J., Cole, S., & Lee, C. (2021, 4). Comparing Observations and Parameterizations of Ice-Ocean Drag Through an Annual Cycle Across the Beaufort Sea. *Journal of Geophysical Research: Oceans*, *126*(4). doi: 10.1029/2020JC016977

Brenner, S., Rainville, L., Thomson, J., & Lee, C. (2020, 1). The evolution of a shallow front in the Arctic marginal ice zone. *Elementa: Science of the Anthropocene*, *8*(1). Retrieved from `/elementa/article/doi/10.1525/elementa.413/112765/The-evolution-of-a-shallow-front-in-the-Arctic` doi: 10.1525/ELEMENTA.413

Cavalieri, D. J., Crawford, J. P., Drinkwater, M. R., Eppler, D. T., Farmer, L. D., Jentz, R. R., & Wackerman, C. C. (1991). Aircraft active and passive microwave validation of sea ice concentration from the Defense Meteorological Satellite Program special sensor microwave imager. *Journal of Geophysical Research*, *96*(C12). Retrieved from `http://doi.wiley.com/10.1029/91JC02335` doi: 10.1029/91JC02335

Collins, C. O., & Rogers, W. E. (2017). *A source term for wave attenuation by sea ice in WAVEWATCH III®: IC4 (Tech. Rep. NRL/MR/7320–17–9726)* (Tech. Rep.). Naval Research Laboratory MS: Stennis Space Center.

Collins, C. O., Rogers, W. E., Marchenko, A., & Babanin, A. V. (2015). In situ measurements of an energetic wave event in the Arctic marginal ice zone. *Geophysical Research Letters*, *42*(6). doi: 10.1002/2015GL063063

Comiso, J. C., Cavalieri, D. J., Parkinson, C. L., & Gloersen, P. (1997). Passive microwave algorithms for sea ice concentration: A comparison of two techniques. *Remote Sensing of Environment*, *60*(3). doi: 10.1016/S0034-4257(96)00220-9

Fetterer, F. (2002). *Sea Ice Index: Interpretation Resources for Sea Ice Trends and Anomalies* (Tech. Rep.). NSIDC Informal Technical Report. Retrieved from `https://nsidc.org/sites/nsidc.org/files/technical-references/Interpretation-Resources-for-Sea-Ice-Trends-and-Anomalies.pdf`

Fetterer, F., Knowles, K., Meier, W. N., Savoie, M., & Windnagel, A. K. (2017). *Sea Ice Index, Version 3. NOAA/NSIDC Climate Data Record of Passive Microwave Sea Ice Concentration.* Boulder, Colorado USA. Retrieved from `https://nsidc.org/data/G02135/versions/3` doi: 10.7265/N5K072F8

Hasselmann, K., Barnett, T. P., Bouws, E., Carlson, H., Cartwright, D. E., Eake, K., ... Walden, H. (1973). *Measurements of wind-wave growth and swell decay during the joint North Sea wave project (JONSWAP).*

Herbers, T. H., Jessen, P. F., Janssen, T. T., Colbert, D. B., & MacMahan, J. H. (2012, 7). Observing ocean surface waves with GPS-tracked buoys. *Journal of Atmospheric and Oceanic Technology*, *29*(7), 944–959. Retrieved from `https://journals.ametsoc.org/view/journals/atot/29/7/jtech-d-11-00128_1.xml` doi: 10.1175/JTECH-D-11-00128.1

Horvat, C., Blanchard-Wrigglesworth, E., & Petty, A. (2020). Observing Waves in Sea Ice With ICESat-2. *Geophysical Research Letters*. doi: 10.1029/2020GL087629

Horvat, C., & Tziperman, E. (2015). A prognostic model of the sea-ice floe size and thickness distribution. *Cryosphere*. doi: 10.5194/tc-9-2119-2015

Horvat, C., Tziperman, E., & Campin, J. M. (2016). Interaction of sea ice floe size, ocean eddies, and sea ice melting. *Geophysical Research Letters*. doi: 10.1002/2016GL069742

Hunke, E. C., Lipscomb, W. H., Turner, A. K., Jeffery, N., & Elliot, S. (2015). CICE : the Los Alamos Sea Ice Model Documentation and Software User's Manual Version 5.1 LA-CC-06-012. *Los Alamos National Laboratory Tech. Rep. LA-CC-06-012*(March 17).

Japan Meteorological Agency, Japan. (2013). *JRA-55: Japanese 55-year Reanalysis, Daily 3-Hourly and 6-Hourly Data.* Boulder CO: Research Data Archive at the National Center for Atmospheric Research, Computational and Information Systems Laboratory. Retrieved from `https://doi.org/10.5065/D6HH6H41`

Johnson, M. A., Marchenko, A. V., Dammann, D. O., & Mahoney, A. R. (2021, 4). Observing Wind-Forced Flexural-Gravity Waves in the Beaufort Sea and Their Relationship to Sea Ice Mechanics. *Journal of Marine Science and Engineering 2021, Vol. 9, Page 471*, *9*(5), 471. Retrieved from `https://www.mdpi.com/2077-1312/9/5/471/htmhttps://www.mdpi.com/2077-1312/9/5/471` doi: 10.3390/JMSE9050471

Kobayashi, S., Ota, Y., Harada, Y., Ebita, A., Moriya, M., Onoda, H., ... Kiyotoshi, T. (2015). The JRA-55 reanalysis: General specifications and basic characteristics. *Journal of the Meteorological Society of Japan*, *93*(1). doi: 10.2151/jmsj.2015-001

Kohout, A. L., Meylan, M. H., & Plew, D. R. (2011). Wave attenuation in a marginal ice zone due to the bottom roughness of ice floes. *Annals of Glaciology*, *52*(57 PART 1). doi: 10.3189/172756411795931525

Kohout, A. L., Williams, M. J., Dean, S. M., & Meylan, M. H. (2014, 5). Storm-induced sea-ice breakup and the implications for ice extent. *Nature*, *509*(7502), 604–607. Retrieved from `https://www.nature.com/articles/nature13262` doi: 10.1038/nature13262

Krishfield, R. A., Proshutinsky, A., Tateyama, K., Williams, W. J., Carmack, E. C., McLaughlin, F. A., & Timmermans, M. L. (2014, 2). Deterioration of perennial sea ice in the Beaufort Gyre from 2003 to 2012 and its impact on the oceanic freshwater cycle. *Journal of Geophysical Research: Oceans*, *119*(2), 1271–1305. Retrieved from `http://www.whoi.edu/beaufortgyre` doi: 10.1002/2013JC008999

Kuik, A. J., van Vledder, G. P., & Holthuijsen, L. H. (1988). A Method for the Routine Analysis of Pitch-and-Roll Buoy Wave Data. *Journal of Physical Oceanography*, *18*(7). doi: 10.1175/1520-0485(1988)018⟨1020:amftra⟩2.0.co;2

Langhorne, P. J., Squire, V. A., Fox, C., & Haskell, T. G. (1998). Break-up of sea ice by ocean waves. *Annals of Glaciology*, *27*. doi: 10.3189/S0260305500017869

Lenain, L., & Melville, W. K. (2017). Measurements of the directional spectrum across the equilibrium saturation ranges of wind-generated surface waves. *Journal of Physical Oceanography*, *47*(8). doi: 10.1175/JPO-D-17-0017.1

Li, J., Kohout, A. L., & Shen, H. H. (2015). Comparison of wave propagation through ice covers in calm and storm conditions. *Geophysical Research Letters*, *42*(14). doi: 10.1002/2015GL064715

Liu, Q., Babanin, A. V., Zieger, S., Young, I. R., & Guan, C. (2016). Wind and wave climate in the Arctic Ocean as observed by altimeters. *Journal of Climate*, *29*(22). doi: 10.1175/JCLI-D-16-0219.1

Marko, J. R. (2003). Observations and analyses of an intense waves-in-ice event in the Sea of Okhotsk. *Journal of Geophysical Research: Oceans*, *108*(9). doi: 10.1029/2001jc001214

Martin, T., Steele, M., & Zhang, J. (2014). Seasonality and long-term trend of Arctic Ocean surface stress in a model. *Journal of Geophysical Research: Oceans*, *119*(3). doi: 10.1002/2013JC009425

Masson, D., & Leblond, P. H. (1989). Spectral evolution of wind-generated surface gravity waves in a dispersed ice field. *Journal of Fluid Mechanics*, *202*(12). doi: 10.1017/S0022112089001096

Mellor, G. L., Steele, M., & McPhee, M. G. (1986). Ice-seawater turbulent boundary layer interaction with melting or freezing. *J. PHYS. OCEANOGR.*, *16*(11 , Nov. 1986). doi: 10.1175/1520-0485(1986)016⟨1829:istbli⟩2.0.co;2

Meylan, M. H., Bennetts, L. G., & Kohout, A. L. (2014). In situ measurements and analysis of ocean waves in the Antarctic marginal ice zone. *Geophysical Research Letters*, *41*(14). doi: 10.1002/2014GL060809

Meylan, M. H., Bennetts, L. G., Mosig, J. E., Rogers, W. E., Doble, M. J., & Peter, M. A. (2018). Dispersion relations, power laws, and energy loss for waves in the marginal ice zone. *Journal of Geophysical Research: Oceans*, *123*(5). doi: 10.1002/2018JC013776

Meylan, M. H., Horvat, C., Bitz, C. M., & Bennetts, L. G. (2021, 5). A floe size dependent scattering model in two- and three-dimensions for wave attenuation by ice floes. *Ocean Modelling*, *161*, 101779. Retrieved from https://linkinghub.elsevier.com/retrieve/pii/S1463500321000299 doi: 10.1016/j.ocemod.2021.101779

Meylan, M. H., & Squire, V. A. (1994). The response of ice floes to ocean waves. *Journal of Geophysical Research*, *99*(C1), 891. Retrieved from http://doi.wiley.com/10.1029/93JC02695 doi: 10.1029/93JC02695

Montiel, F., Squire, V. A., & Bennetts, L. G. (2016, 3). Attenuation and directional spreading of ocean wave spectra in the marginal ice zone. *Journal of Fluid Mechanics*, *790*, 492–522. Retrieved from https://www.cambridge.org/core/product/identifier/S0022112016000215/type/journal_article doi: 10.1017/jfm.2016.21

Notz, D., & Community, S. (2020, 5). Arctic Sea Ice in CMIP6. *Geophysical Research Letters*, *47*(10), e2019GL086749. Retrieved from https://onlinelibrary.wiley.com/doi/full/10.1029/2019GL086749https://onlinelibrary.wiley.com/doi/abs/10.1029/2019GL086749https://agupubs.onlinelibrary.wiley.com/doi/10.1029/2019GL086749https://onlinelibrary.wiley.com/doi/10.1029/2019GL086749 doi: 10.1029/2019GL086749

Phillips, O. M. (1985). Spectral and statistical properties of the equilibrium range in wind-generated gravity waves. *Journal of Fluid Mechanics*, *156*. doi: 10.1017/S0022112085002221

Roach, L. A., Bitz, C. M., Horvat, C., & Dean, S. M. (2019). Advances in Modeling Interactions Between Sea Ice and Ocean Surface Waves. *Journal of Advances in Modeling Earth Systems*. doi: 10.1029/2019MS001836

Roach, L. A., Horvat, C., Dean, S. M., & Bitz, C. M. (2018). An Emergent Sea Ice Floe Size Distribution in a Global Coupled Ocean-Sea Ice Model. *Journal of Geophysical Research: Oceans*. doi: 10.1029/2017JC013692

Roach, L. A., Smith, M. M., & Dean, S. M. (2018, 4). Quantifying Growth of Pancake Sea Ice Floes Using Images From Drifting Buoys. *Journal of Geophysical Research: Oceans*, *123*(4), 2851–2866. Retrieved from https://onlinelibrary.wiley.com/doi/10.1002/2017JC013693 doi: 10.1002/2017JC013693

Rogers, W. E., Thomson, J., Shen, H. H., Doble, M. J., Wadhams, P., & Cheng, S. (2016). Dissipation of wind waves by pancake and frazil ice in the autumn Beaufort Sea. *Journal of Geophysical Research: Oceans*. doi: 10.1002/2016JC012251

Rolph, R. J., Feltham, D. L., & Schröder, D. (2020). Changes of the Arctic marginal ice zone during the satellite era. *Cryosphere*, *14*(6). doi: 10.5194/tc-14-1971-2020

Rothrock, D. A., & Thorndike, A. S. (1980). Geometric properties of the underside of sea ice. *Journal of Geophysical Research*, *85*(C7). doi: 10.1029/JC085iC07p03955

Shen, H. H. (2019). *Modelling ocean waves in ice-covered seas* (Vol. 83). doi: 10.1016/j.apor.2018.12.009

Shen, H. H., Ackley, S. F., & Hopkins, M. A. (2001, 9). A conceptual model for pancake-ice formation in a wave field. *Annals of Glaciology*, *33*, 361–367. Retrieved from https://www.cambridge.org/core/product/

identifier/S0260305500264380/type/journal_article doi: 10.3189/172756401781818239

Shen, H. H., Ackley, S. F., & Yuan, Y. (2004). Limiting diameter of pancake ice. *Journal of Geophysical Research C: Oceans*, *109*(12). doi: 10.1029/2003JC002123

Shu, Q., Wang, Q., Song, Z., Qiao, F., Zhao, J., Chu, M., & Li, X. (2020, 5). Assessment of Sea Ice Extent in CMIP6 With Comparison to Observations and CMIP5. *Geophysical Research Letters*, *47*(9), e2020GL087965. Retrieved from https://agupubs.onlinelibrary.wiley.com/doi/full/10.1029/2020GL087965https://agupubs.onlinelibrary.wiley.com/doi/abs/10.1029/2020GL087965https://agupubs.onlinelibrary.wiley.com/doi/10.1029/2020GL087965 doi: 10.1029/2020GL087965

Smith, M., Holland, M., & Light, B. (2021). Arctic sea ice sensitivity to lateral melting representation in a coupled climate model. *The Cryosphere Discussions*(March), 1–21. doi: 10.5194/tc-2021-67

Smith, M., & Thomson, J. (2016). Scaling observations of surface waves in the Beaufort Sea. *Elementa*. doi: 10.12952/journal.elementa.000097

Squire, V. A. (2007). *Of ocean waves and sea-ice revisited* (Vol. 49) (No. 2). doi: 10.1016/j.coldregions.2007.04.007

Squire, V. A. (2018). A fresh look at how ocean waves and sea ice interact. *Philosophical Transactions of the Royal Society A: Mathematical, Physical and Engineering Sciences*, *376*(2129). doi: 10.1098/rsta.2017.0342

Squire, V. A. (2020, 1). Ocean Wave Interactions with Sea Ice: A Reappraisal. *Annual Review of Fluid Mechanics*, *52*(1), 37–60. Retrieved from https://www.annualreviews.org/doi/10.1146/annurev-fluid-010719-060301 doi: 10.1146/annurev-fluid-010719-060301

Squire, V. A., Dugan, J. P., Wadhams, P., Rottier, P. J., & Liu, A. K. (1995, 1). Of Ocean Waves and Sea Ice. *Annual Review of Fluid Mechanics*, *27*(1), 115–168. Retrieved from www.annualreviews.orghttp://www.annualreviews.org/doi/10.1146/annurev.fl.27.010195.000555 doi: 10.1146/annurev.fl.27.010195.000555

Squire, V. A., & Moore, S. C. (1980). *Direct measurement of the attenuation of ocean waves by pack ice [6]* (Vol. 283) (No. 5745). doi: 10.1038/283365a0

Steele, M. (1992). Sea ice melting and floe geometry in a simple ice-ocean model. *Journal of Geophysical Research*, *97*(C11). doi: 10.1029/92jc01755

Stopa, J. E., Sutherland, P., & Ardhuin, F. (2018). Strong and highly variable push of ocean waves on Southern Ocean sea ice. *Proceedings of the National Academy of Sciences of the United States of America*, *115*(23). doi: 10.1073/pnas.1802011115

Strong, C., Foster, D., Cherkaev, E., Eisenman, I., & Golden, K. M. (2017). On the definition of marginal ice zone width. *Journal of Atmospheric and Oceanic Technology*. doi: 10.1175/JTECH-D-16-0171.1

Strong, C., & Rigor, I. G. (2013). Arctic marginal ice zone trending wider in summer and narrower in winter. *Geophysical Research Letters*, *40*(18). doi: 10.1002/grl.50928

The WAVEWATCH III (R) Development Group (WW3DG). (2016). *User manual and system documentation of WAVEWATCH III TM version 5.16* (Tech. Rep. No. 329).

Thomson, J. (2012). Wave breaking dissipation observed with "swift" drifters. *Journal of Atmospheric and Oceanic Technology*. doi: 10.1175/JTECH-D-12-00018.1

Thomson, J. (2020). *Long-term Measurements of Ocean Waves and Sea Ice Draft in the Central Beaufort Sea October 2020* (Tech. Rep. No. APL-UW TM 1-20). Applied Physics Laboratory, University of Washington.

Thomson, J., Ackley, S., Girard-Ardhuin, F., Ardhuin, F., Babanin, A., Boutin, G.,

. . . Wadhams, P. (2018). Overview of the Arctic Sea State and Boundary Layer Physics Program. *Journal of Geophysical Research: Oceans*, *123*(12). doi: 10.1002/2018JC013766

Thomson, J., D'Asaro, E. A., Cronin, M. F., Rogers, W. E., Harcourt, R. R., & Shcherbina, A. (2013). Waves and the equilibrium range at Ocean Weather Station P. *Journal of Geophysical Research: Oceans*, *118*(11). doi: 10.1002/2013JC008837

Thomson, J., Fan, Y., Stammerjohn, S., Stopa, J., Rogers, W. E., Girard-Ardhuin, F., . . . Bidlot, J. R. (2016, 9). Emerging trends in the sea state of the Beaufort and Chukchi seas. *Ocean Modelling*, *105*, 1–12. doi: 10.1016/j.ocemod.2016.02.009

Thomson, J., Gemmrich, J., Rogers, W. E., Collins, C. O., & Ardhuin, F. (2019, 11). Wave Groups Observed in Pancake Sea Ice. *Journal of Geophysical Research: Oceans*, *124*(11), 7400–7411. Retrieved from `https://agupubs-onlinelibrary-wiley-com.offcampus.lib.washington.edu/doi/full/10.1029/2019JC015354https://agupubs-onlinelibrary-wiley-com.offcampus.lib.washington.edu/doi/abs/10.1029/2019JC015354https://agupubs-onlinelibrary-wiley-com.offcampus.lib.wash` doi: 10.1029/2019JC015354

Thomson, J., Girton, J. B., Jha, R., & Trapani, A. (2018). Measurements of directional wave spectra and wind stress from a Wave Glider autonomous surface vehicle. *Journal of Atmospheric and Oceanic Technology*, *35*(2). doi: 10.1175/JTECH-D-17-0091.1

Thomson, J., Hošeková, L., Meylan, M. H., Kohout, A. L., & Kumar, N. (2021). Spurious Rollover of Wave Attenuation Rates in Sea Ice Caused by Noise in Field Measurements. *Journal of Geophysical Research: Oceans*, *126*(3). doi: 10.1029/2020JC016606

Thomson, J., & Rogers, W. E. (2014). Swell and sea in the emerging Arctic Ocean. *Geophysical Research Letters*. doi: 10.1002/2014GL059983

Tietsche, S., Day, J. J., Guemas, V., Hurlin, W. J., Keeley, S. P., Matei, D., . . . Hawkins, E. (2014). Seasonal to interannual Arctic sea ice predictability in current global climate models. *Geophysical Research Letters*, *41*(3). doi: 10.1002/2013GL058755

Toyota, T., Takatsuji, S., & Nakayama, M. (2006). Characteristics of sea ice floe size distribution in the seasonal ice zone. *Geophysical Research Letters*, *33*(2). doi: 10.1029/2005GL024556

Voermans, J. J., Babanin, A. V., Thomson, J., Smith, M. M., & Shen, H. H. (2019). Wave Attenuation by Sea Ice Turbulence. *Geophysical Research Letters*, *46*(12). doi: 10.1029/2019GL082945

Wadhams, P., Squire, V. A., Goodman, D. J., Cowan, A. M., & Moore, S. C. (1988, 6). The attenuation rates of ocean waves in the marginal ice zone. *Journal of Geophysical Research*, *93*(C6), 6799. Retrieved from `http://doi.wiley.com/10.1029/JC093iC06p06799` doi: 10.1029/JC093iC06p06799

Wang, R., & Shen, H. H. (2010). Gravity waves propagating into an ice-covered ocean: A viscoelastic model. *Journal of Geophysical Research: Oceans*, *115*(6). doi: 10.1029/2009JC005591

Wang, X. L., Feng, Y., Swail, V. R., & Cox, A. (2015). Historical changes in the Beaufort-Chukchi-Bering Seas surface winds and waves, 1971-2013. *Journal of Climate*, *28*(19). doi: 10.1175/JCLI-D-15-0190.1

Williams, T. D., Bennetts, L. G., Squire, V. A., Dumont, D., & Bertino, L. (2013). Wave-ice interactions in the marginal ice zone. Part 1: Theoretical foundations. *Ocean Modelling*, *71*. doi: 10.1016/j.ocemod.2013.05.010

Young, I. R. (1999). *Wind generated ocean waves*. Elsevier.